Aug. 30, 2017

Feasibility study of the OST transit spectrograph

Taro Matsuo (Osaka University)

1. Summary

We investigated the final noise floor for the OST transit spectrograph, considering the following systematic noises: 1. image movement on intra- and inter-pixel sensitivity variations, 2. PSF movement on a field stop (i.e., slit loss) and spatial filtering due to finite optical elements, and 3. gain fluctuations generated in a detector and readout circuit. The above three factors mainly limit the performances of transit photometry and spectroscopy on the current and near-term space observatories. We evaluated the photometric errors induced by the three factors for the current design of the OST transit spectrograph and then found that the final noise floor is mainly limited by the slit loss; the impact of the inter-pixel response on the photometric stability is negligible thanks to a number of the science pixels. We also noticed that the gain fluctuations can be calibrated with two types of the reference pixels: “onboard” and “outboard” reference pixels, which are not irradiated by any science light and thermal background radiation. The calibration technique successfully reduces the gain fluctuation to Gaussian random noise under some appropriate assumptions. Given that the detector gain is correctly calibrated with the reference pixels, the final noise floors over the entire wavelength range of 6 to 25μm are 3, 5, and 20 ppm under the telescope pointing jitters of 8, 10, and 20 mas, respectively. We will build a prototype of the OST transit spectrograph and evaluate the real final noise floor through a testbed, which will be built at the NASA Ames Research Center next year.

In this document, the current design of the OST transit spectrograph is first introduced and the impact of each systematic noise on the photometric stability is mathematically described. The final noise floor is quantitatively derived under some appropriate assumptions. We also attached the following Appendixes at the end of this document for more information: pupil masks for reduction of slit loss (Appendix A), analysis of wavefront propagation (Appendix B), modelling of detector and readout electronics (Appendix C), and calibration of detector gain with reference pixels (Appendix D). In addition, all of the parameters and assumptions used in this report are compiled in Appendix E.

2. Conceptual design

The OST transit spectrograph is designed based on the densified pupil spectroscopy (Matsuo et al. 2016), which performs high stable spectrophotometry against telescope pointing jitter and deformation of primary mirror. The optical system mainly composed of four parts: 1. relay optical system, 2. pupil remapping and densification part, 3. spectrograph, and 4. detector and readout circuit. Figures 1 shows the block diagram of the OST transit spectrograph. Figures 2 and 3 show its overall view and the enlarged view of the optical system from the pupil slicer to the detectors, respectively. The transmittance of the OST transit spectrograph except for the dichroic mirrors and detector is expected to be more than 80% over the entire wavelength range of 6-25μm. The specifications of the dichroic mirrors, which divide white light into the three wavelength ranges, 6-11μm, 11-18μm, and 18-25μm, are not determined because several Japanese filter makers I contacted cannot produce them due to the wide wavelength range. We need to contact to filter makers in U.S. and Europe. The key components in the OST transit spectrograph are briefly introduced in the next subsections.

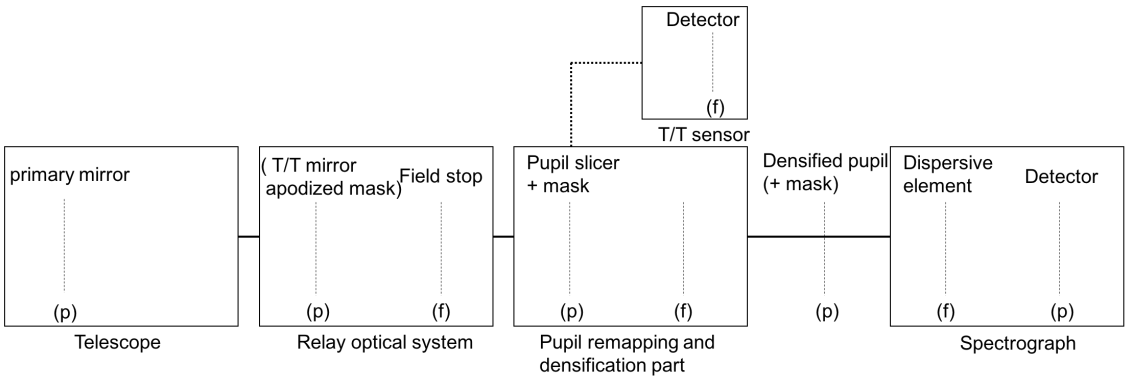

Figure 1. Block diagram of the current OST transit spectrograph. (p) and (f) represent the pupil and focal planes, respectively. The light from one segmented mirror, corresponding to 2.7% of all amount of light, is used for monitor of the telescope pointing jitter. The specification of the tip-tilt sensor is not determined.

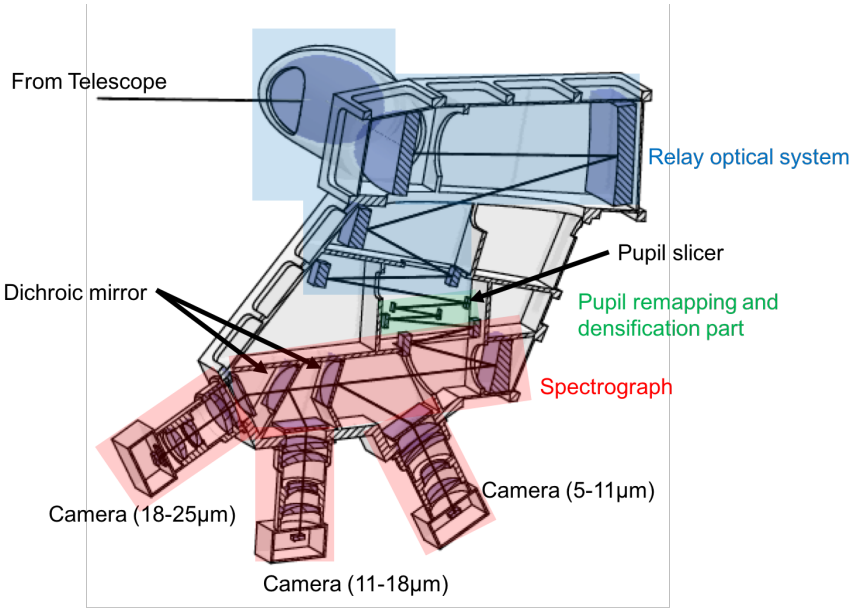

Figure 2. Overall view of the current OST transit spectrograph. The blue-, green-, and red-colored areas show the relay optical system, the pupil remapping and densification part, and the spectrograph, respectively.

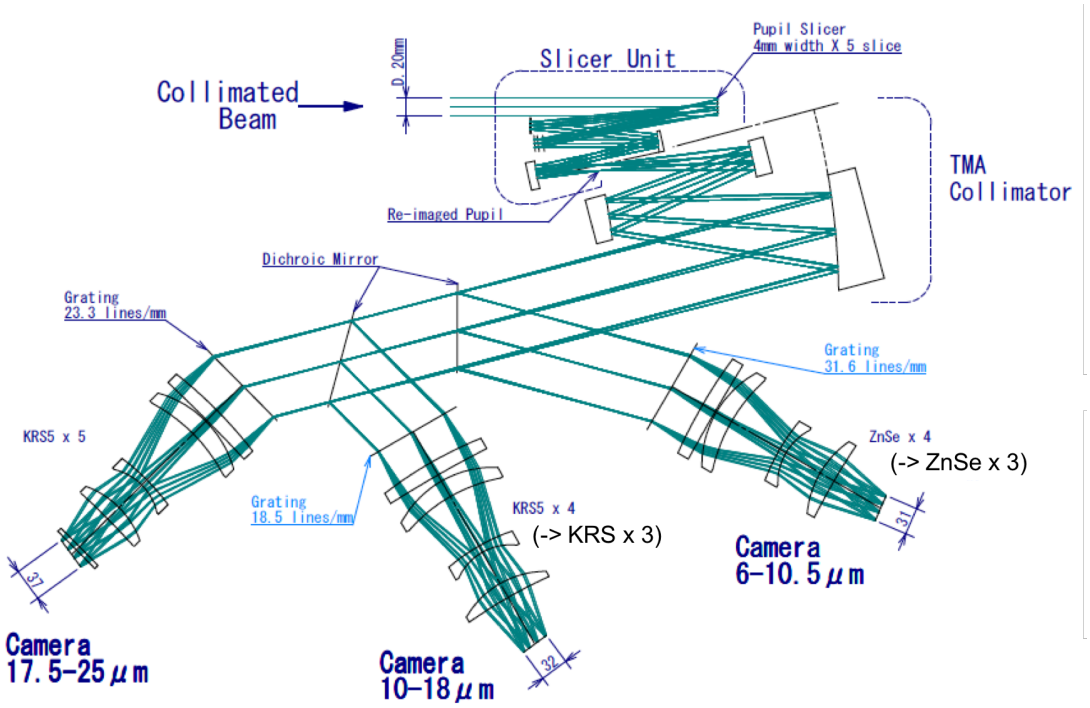

Figure 3. Enlarged view of the pupil remapping and densification part and spectrograph. The camera lens system will be simplified because the optical aberration does not largely contribute to the final noise floor. The number of the camera lenses for each wavelength range is reduced to two or three.

2.1. Field stop

The relay optical system includes both of pupil and focal planes. A field stop puts on the focal plane to remove background stars and to minimize thermal background from zodiacal light. As explained in Section 3.2.2, the field stop radius is determined such that the slit loss due to the field stop induced by the telescope pointing jitter is comparable to that by the dispersive element put on the focal plane just before the detector plane. The field stop radius is set to 2.5 arcsec, corresponding to 8 λ/D at 24 μm for the 9.3m OST primary mirror. The photometric variation due to the slit loss is expected to be less than 5 ppm under the pointing jitter of 10 mas. If the pointing jitter of the OST telescope is larger than expected, there are the following three choices;

1. Without any change

The photometric stability is less degraded than expected without any measure, given that the pointing jitter is symmetry to some extent. In addition, because the pointing jitter can be simultaneously monitored (see next subsection), we may be able to estimate the number of the photons reduced due to the slit loss.

2. Real-time control

The telescope pointing jitter is suppressed by a tip-tilt mirror put on the pupil plane in the relay optical system through monitoring of the image movement on a tip-tilt sensor.

3. Pupil mask

An apodized pupil mask employs such that the image pattern matches to the radius of the field stop (see Appendix A3; Itoh et al. 2017). Note that, because the optical transmissivity decreases because of the limited efficiency of the pupil mask, the pupil mask should be designed such that the photometric error due to the photon noise is comparable to the slit-loss variation.

Once the frequency spectrum of the OST pointing jitter is determined, we will perform numerical simulations for the photometric stability due to the slit loss and study which choice is suitable for the OST transit spectrograph.

2.2. Pupil slicer

The pupil remapping is performed by a pupil slicer put on the pupil plane, which is optically conjugated to the OST primary mirror. Figure 4 shows the conceptual diagram of the pupil slicer. The pupil slicer plays the following three important roles in

improvement of the photometric stability. First, the pupil is remapped by the pupil slicer and the science light is spread over broad area of the detector plane. The pupil remapping leads to largely mitigate the systematic noise produced due to image movement on the intra- and inter-pixel sensitivity variations.

Second, the pupil slicer is designed such that an impact of the segmented mirror on the photometric stability is minimized. Since the optical performance for the edge of the segmented mirror is generally degraded, the scattered light generated by the edge spreads over the entire detector plane and leads to a limitation of the photometric stability. As shown in Figure 4, the pupil is divided in tune with the figure of the segmented mirror and a mask for hiding the edge employs. The division number for the current design is 6. The light from the remaining one segmented mirror (represented by the red circle in Figure 4) is used for monitor of the telescope pointing jitter.

Finally, a mask put at the outer side of the pupil slicer shields “cold pixels” from thermal radiation nearby the primary mirror. Since the detector plane is optically conjugated to the pupil slicer, the pixels out of the science light on the detector plane are not irradiated by any thermal source. Only dark current produced by leakages inside the photoconductor is observed in these cold pixels, which we call “onboard reference pixels.” The blue-colored region also includes “outboard reference pixels,” in which neither electric charges induced by incident flux nor dark current is generated. The gain fluctuations in the detector and readout circuit can be calibrated with the two types of reference pixels. Note that, instead of the mask out of the pupil slicer, a mask on the densified pupil after the pupil remapping and densification part can also work for protection of the reference pixels from the thermal background light.

2.3. Pupil densification

The pupil densification has a key role in performing stable spectroscopy. The densification factor is multiplication of the division number of the pupil slicer and the pupil densification by the two aspheric mirrors after the pupil slicer (see Figure 3). The densified subpupils after the pupil densification part correspond to the entrance of the spectrograph. Thanks to the large densification factor, each densified subpupil acts as a point source and each beam is collimated by the first three aspheric mirrors. The dispersive device put in the collimated beam spreads the light in one dimension as a function of the wavelength. As a result, the OST transit spectrograph performs stable

spectroscopy even with the dispersive element put on the focal plane. Thus, the spectroscopy done by the OST transit instrument is essentially same as those of existing focal-plane spectrographs.

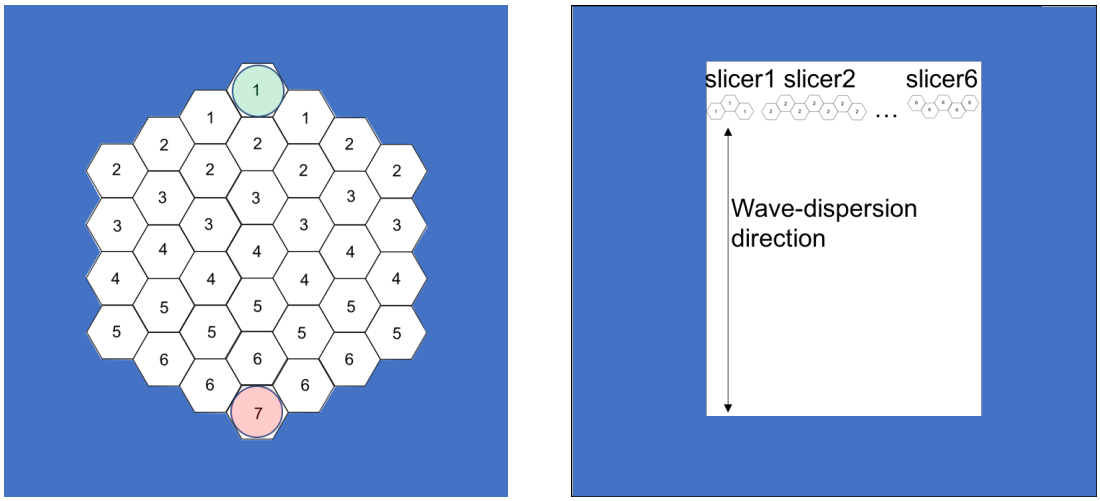

Figure 4. Conceptual design of pupil slicer (left) and science and reference pixels on detector plane (right).

(left) The number printed on each segment mirror indicates which slicer each segment mirror belongs to. The blue-colored region indicates a cold photon-shield mask. The green circle represents a mask for hiding the edge of the segmented mirror. The light from the segmented mirror belonging to the seventh sub-group, indicated by the red circle, is used for monitor of the telescope pointing jitter.

(right) The blue-colored region is shielded by the pupil mask outside of the pupil slicer. According to the current design for the 5-18μm wavelength range, the areas of the science and reference pixels are roughly 400 x 1000 and 1600 x 2000 + 400 x 1000, respectively.

2.4. Two types of reference pixels

As described before, there are two types of the reference pixels, “onboard” and “outboard” reference pixels, in the blue-colored region shown in Figure 4. Note that the outboard reference pixels used here are different with those prepared for the wide field camera on Hubble Space Telescope (Robberto et al. 2002). While the former is shielded from any thermal radiation with a cold mask put on the pupil plane, the latter does not apply indium bumping, which connects a Si:As focal plane array with a Si readout integrated circuit (ROIC). As a result, both the dark current and offset voltage are

generated in the onboard reference pixel and only the offset voltage is observed on the outboard reference pixel. As described in Appendix D, the offset voltages occurred in both of the science and onboard reference pixels are removed by use of the outboard reference pixels. In addition, the gain fluctuation generated in the detector and readout electronics is in principal calibrated with the subtracted onboard reference pixels because most of the fluctuations are common to all of the detector pixels.

Figure 5 shows a configuration example for the science pixels and two types of reference pixels. This configuration is optimized for subtraction of vertical stripes (i.e., offset voltage) occurred by the multiplexers.

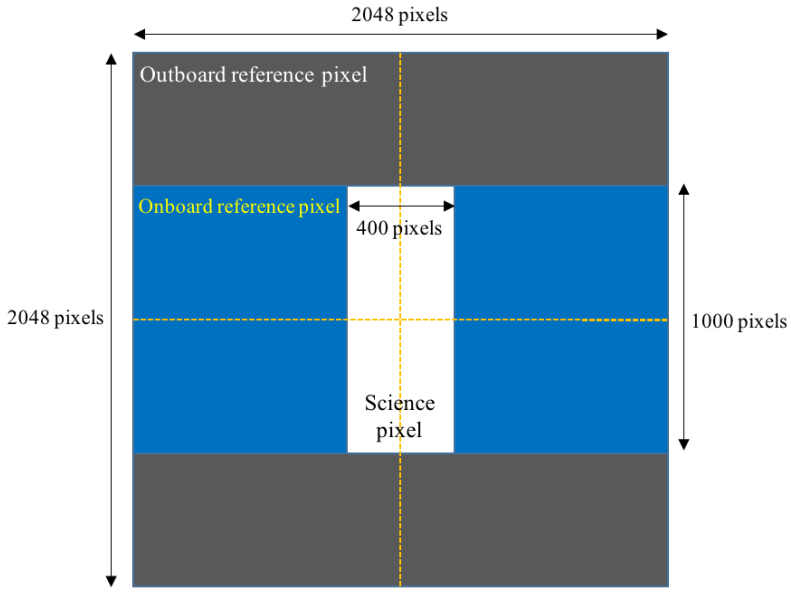

Figure 5. Configuration example of science and two types of reference pixels. The white-, blue-, and black-colored regions represent the science, onboard reference, and outboard reference pixels, respectively. The numbers of the science, onboard reference, and outboard reference pixels are, respectively, $4x10^5$, $1.6x10^6$, and $2.0x10^6$. Given that vertical stripes are mainly produced by the multiplexers, the outboard reference pixels are arranged horizontally.

3. Evaluation of each systematic noise floor

In this section, we briefly formulate the observing signal for general transit observations and then clarify how each systematic noise contributes to the final noise floor of the transit observations. We derive the final noise floor of the OST transit

spectrograph under some appropriate assumptions. Note that the detailed model for the detector and readout circuit is described in Appendix C.

3.1. Formulation

3.1.1. pixel value

Figure 6 shows a block diagram for general transit observations. The signal value of the *i*-th science pixel with the *j*-th multiplexer (MUX) and readout circuit as a function of time, $D_{sci,i,j}(t)$, is simply described by the following Equation:

$$D_{sci,i,j}(t) = (fO_i + Q_i)g_{i,j} + V_{i,j} + \sigma_{sci,i,j}, \quad (1)$$

where f is number of the incident photons into a sub-region of the primary mirror corresponding to one detector pixel, Q is electric charge corresponding to dark current, O shows optical transmissivity including quantum efficiency, g is gain from electric charge to voltage before analog-to-digital conversion, V is offset voltage, and σ is random noise. The subscripts of i and j represent physical quantities attached to the *i*-th pixel and the *j*-th MUX and readout circuit. The offset voltage is produced in a conversion process from electron to voltage in each pixel, a multiplexer, and a readout circuit, and is mathematically described by superposition of Equations (C4) and (C8). The random noise attached to the *i*-th pixel is represented by Equation (C9). Since each term except for the random noise and offset voltage is decomposed into the average and fluctuation terms, Equation (1) is written as

$$\begin{aligned} D_{sci,i,j}(t) = {} & \{(\langle f\rangle_t + \delta f)(\langle O_i\rangle_t + \delta O_i) + (\langle Q_i\rangle_t + \delta Q_i)\}\left(\langle g_{i,j}\rangle_t + \delta g_{i,j}\right) \\ & + \langle V_{i,j}\rangle_t + \delta V_{i,j} + \sigma_{sci,i,j}, \end{aligned} \quad (2)$$

where $\langle A\rangle_t$ and δA represent average value and fluctuation of A along the axis of time. Note that $\langle f\rangle_t + \delta f$ is common to all the science pixels for the case of the OST transit spectrograph. When each fluctuation term is much smaller than the first-order fluctuation terms, the second- and third-order fluctuation terms, $\delta f \delta O_i$, $\delta O_i \delta g_{i,j}$, $\delta f \delta g_{i,j}$, $\delta g_{i,j}\delta Q_i$and $\delta f \delta g_{i,j}\delta O_i$, are negligible:

$$\begin{aligned} D_{sci,i,j}(t) \approx {} & (\langle f\rangle_t\langle O_i\rangle_t + \langle Q_i\rangle_t)\langle g_i\rangle_t + \langle g_i\rangle_t(\langle O_i\rangle_t\delta f + \langle f\rangle_t\delta O_i + \delta Q_i) \\ & + (\langle f\rangle_t\langle O_i\rangle_t + \langle Q_i\rangle_t)\delta g_i + \left(\langle V_{i,j}\rangle_t + \delta V_{i,j}\right) + \sigma_{sci,i,j}. \end{aligned} \quad (3)$$

The first and third terms on the right-hand side of Equation (3), respectively, represent the average value of the science pixel value and the fluctuations of the gain amplitudes occurred in the detector and readout circuit. The first and third terms are in detail

mathematically described by Equations (C3) and (C5), respectively. When the average value of the *i*-th science pixel value is normalized to 1, Equation (3) is reduced to

$$\widetilde{D_{sci,i,j}}(t) \equiv \frac{D_{sci,i,j}(t)}{(\langle f\rangle_t\langle O_i\rangle_t+\langle Q_i\rangle_t)\langle g_{i,j}\rangle_t}$$

$$\approx 1+\frac{\delta f}{\langle f\rangle_t}+\frac{\delta O_i}{\langle O_i\rangle_t}+\frac{\delta Q_i}{\langle f\rangle_t\langle O_i\rangle_t}+\frac{\delta g_{i,j}}{\langle g_{i,j}\rangle_t}+\frac{(\langle V_{i,j}\rangle_t+\delta V_{i,j})}{\langle f\rangle_t\langle O_i\rangle_t\langle g_{i,j}\rangle_t}+\frac{\sigma_{sci,i,j}}{\langle f\rangle_t\langle O_i\rangle_t\langle g_{i,j}\rangle_t}, \quad (4)$$

where we assume that $\langle Q_i\rangle_t$ is much smaller than $\langle f\rangle_t\langle O_i\rangle_t$. $\frac{\delta O_i}{\langle O_i\rangle_t}$ and $\frac{\delta g_{i,j}}{\langle g_{i,j}\rangle_t}$ represent the variations of the optical transmissivity and detector gain attached to the *i*-th science pixel, respectively. Thus, the value of the *i*-th science pixel is decomposed into superposition of the transit signal, fluctuation term, and random noise.

3.1.2. Noise floor for each spectral component

In the OST transit spectrograph, a spectrally resolved component is not observed by a few pixels but by a number of pixels, and the number of the samplings for each spectral component is almost same over the entire wavelength range of 6-25μm. Given that the number of the samplings for each spectrally resolved component on the detector is n_{sci}, the fluctuation and random noise terms are averaged over the number of pixels irradiated by the same spectral component. According to the current design of the OST transit spectrograph, the number of the science pixels for a component with a spectral resolution of 100 is approximately 3600. Because each fluctuation term is statistically independent of each other, the final noise floor for each spectral component can be written as the root sum square of the two fluctuation terms and the random noise:

$$\widetilde{\delta D_{sci}} \approx \sqrt{\left(\langle\frac{\delta O_i}{\langle O_i\rangle_t}\rangle_{n_{sci}}\right)^2+\left(\langle\frac{\delta g_{i,j}}{\langle g_{i,j}\rangle_t}\rangle_{n_{sci}}\right)^2+\left(\langle\frac{\sigma_{sci,i,j}}{\langle f\rangle_t\langle O_i\rangle_t\langle g_i\rangle_t}\rangle_{n_{sci}}\right)^2}, \quad (5)$$

where we assume that the variation of the offset voltage induced by the gain fluctuation, $\delta V_{i,j}$, is not considered because it can be estimated from the outboard reference pixels, in which only the offset voltage is generated. The first term on the right-hand side in Equation (5) represents the photometric error occurred by any optical aberration such as the telescope pointing jitter and distortion of the primary mirror. The photometric variation due to the slit loss and image movement on the intra- and inter-pixel sensitivity

variations are included in $\frac{\delta O_i}{\langle O_i \rangle}$. The second term is mainly caused by the fluctuations of the detector bias voltage and temperature in the detector and readout electronics. Regarding the third term, because $\langle O_i \rangle_t \langle g_{i,j} \rangle_t$ is a constant of order unity and $\sigma_{sci,i,j}$ becomes $\sigma_{photon,i}$ for observation of a bright star, the third term shows the photon noise fluctuation, which is the principal limit on the transit observations. In the following subsections, we evaluate each fluctuation term.

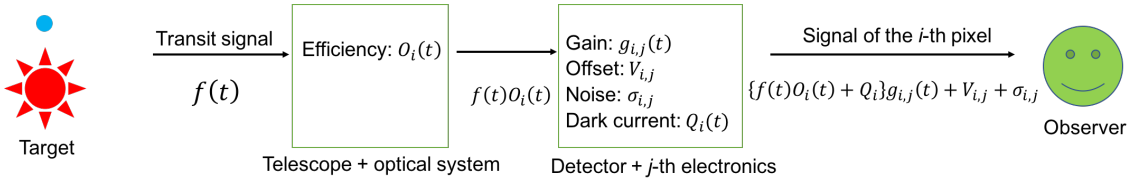

Figure 6. Block diagram for the i-th science pixel with the j-th MUX and readout circuit. The efficiency includes both the optical transmissivity and quantum efficiency of the detector.

3.2. Optical stability

3.2.1. Intra- and inter-pixel sensitivity variation

We first evaluate the photometric fluctuation induced by image movement on the intra- and inter-pixel sensitivity variations. Based on the previous studies (e.g., Greene 2013; ARIEL M4 proposal), when the FWHM of PSF is sampled by more than two pixels, the photometric stability induced by the telescope pointing jitter is not limited by the intra-pixel response but by the inter-pixel one. Because the number of the science pixels for the current OST transit spectrograph is much larger than 2, an impact of the intra-pixel sensitivity variation on the photometric stability is negligible compared to that of the inter-pixel sensitivity variation. According to Matsuo et al. (2016), the standard deviation of the photometric stability due to the inter-pixel response is represented by

$$\left(\frac{\delta O}{\langle O \rangle_t}\right)_{inter} \approx \frac{\sqrt{2N_{motion}}\sigma_{inter}}{n_{sci}^2}, \tag{8}$$

where N_{motion} and σ_{inter} are the number of pixels newly irradiated or not newly irradiated by image motion and the standard deviation of the inter-pixel sensitivity variation, respectively. As n_{sci} increases, the influence of the inter-pixel response on the photometric stability largely decreases.

We performed detailed wavefront analysis for the OST transit spectrograph to derive the image movement on the focal plane, N_{motion}, for various magnitudes of the telescope pointing jitters (see Appendix B). The pupil displacements on the detector plane due to the image motion are less than 0.15 pixel under the telescope pointing jitters smaller than 40 mas, corresponding to 0.1 λ/D at 20μm. Given that σ_{inter} is set to 0.4% (Deming et al. 2009), the photometric error is much smaller than 1ppm. Thus, the impact of the inter-pixel sensitivity response on the photometric error can be negligible even for the large telescope pointing jitter, thanks to a number of the science pixels.

Table 1. Image movements for various magnitudes of the telescope pointing jitter.

Tilt x (mas)	0	8	0	24	0	40
Tilt y (mas)	8	0	24	0	40	0
Displacement in x (pixel)	0.1	0.07	0.08	0.15	0.07	0.11
Displacement in y (pixel)	0.07	0.06	0.04	0.13	0.22	0.04

Note. x and y axes correspond to the spatial and spectral those. The pixel size is set to 30μm.

3.2.2. Slit loss

We next evaluate the photometric error due to the field stop loss and spatial filtering of the optical components induced by the telescope pointing jitter. The slit loss occurs in the following two components: 1. field stop put on the first focal plane in the relay optical system and 2. dispersive element put on the final focal plane in the spectrograph. Figure 6 shows the photometric error as functions of the pointing jitter and the field stop radius. While there is a positive correlation between the photometric error and the pointing jitter, a negative relation between the photometric error and the field stop radius exists. As a result, the impact of the slit loss on the photometric stability does not strongly depend on the observing wavelength. Note that the photometric error is mathematically described by Equation (A1).

The OST transit spectrograph is designed such that the slit loss variations occurred by the above two optical components, the field stop and dispersive element, are comparable; both their radii are set to about 4 λ/D at 25μm. The red dotted line represents the photometric error due to the slit loss induced by the telescope pointing jitter for the current

OST transit spectrograph. The noise floors over the entire wavelength range of 6 to 25μm are 3, 5, and 20 ppm for the pointing jitters of 8, 10, and 20 mas, respectively. Note that an effect of PSF degradation induced by optical aberration is not included in the current numerical simulation and the photometric error due to the slit loss is expected to increase (see Appendix A3).

The photometric instability induced by the telescope pointing jitter is not generated only by the field stop put on the focal plane but also by all the optical elements except for the pupil slicer on the pupil plane. To evaluate the photometric error due to the spatial filtering of the optical elements, we performed wavefront analysis of the OST transit spectrograph with spectrum of plane wave (SPW), which calculates the wavefront propagation with an accuracy of physical optics. As shown in Figure B2, the simulated intensity distribution on the detector plane at wavelength of 20μm has a periodic pattern, which is formed by a two-dimensional convolution of the input pupil function with Fourier transform of the field stop and the optical elements put near the focal plane. Based on the number of the periodic pattern observed in the numerical simulations, we confirmed that the impact of the spatial filtering due to the optical elements on the photometric stability is smaller than one induced by the slit loss of the field stop. Thus, the photometric error due to the slit loss and spatial filtering is a few ppm under the telescope pointing jitter of 10 mas. We will perform additional wavefront analysis with SPW and directly derive the photometric accuracy.

3.3. Gain amplitudes of detector and readout electronics

3.3.1. Performance without any calibration

In this section, we consider an impact of the gain fluctuations generated in the detector and readout electronics on the photometric stability. As explained in Appendix D, because the gain fluctuations do not act randomly, the gain fluctuations are not smoothed out even through a summation process of the observation data. In addition, the densified pupil spectroscopy, which is the basis of the OST transit spectrograph, cannot reduce the photometric error due to the gain fluctuations because the data of the science pixels are commonly affected by them. The variation of the gain amplitude is the fundamental limitation on the photometric stability for the OST transit spectrograph. Given that the variation of the gain amplitude is 500ppm at maximum, the photometric accuracy is limited to a few hundred ppm (see Figure D5).

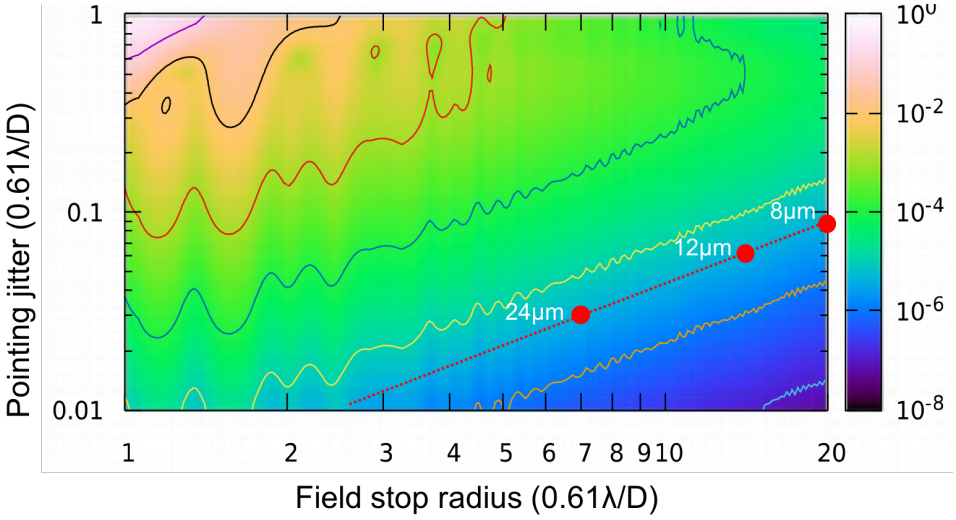

Figure 7. Photometric error due to slit loss induced by telescope pointing jitter. The red dotted line shows the noise floor for the OST transit spectrograph. The pointing jitter is set to 10 mas. We do not consider an impact of the PSF degradation due to any optical aberration on the photometric stability.

3.3.2. Calibration of gain fluctuations with reference pixels

We develop a method for calibration of the gain fluctuations in real time with the two types of reference pixels; onboard and outboard reference pixels, which are with and without connection between the Si:As focal plane array and the Si ROIC through indium bump, respectively, and are not exposed by any science light and thermal background radiation thanks to the cold photon-shield mask out of the pupil slicer. The process of the calibration method is mainly composed of the following two: 1. subtraction of the offset voltage from both of the science and onboard reference pixels, and 2. subtraction of the subtracted onboard reference pixel from the subtracted science one. In terms of the first process, because only the offset voltage is measured from the outboard reference pixels, the contributions of the offset voltage to the science pixels and the onboard reference pixels can be removed. As a result, the subtracted onboard reference pixel data precisely traces the gain fluctuations; the data corresponds to the product of the dark current and the gain amplitudes (Appendix D1). In the second process, the gain fluctuation in the subtracted science pixel data is expected to be precisely corrected through subtraction of the subtracted onboard reference pixel from the subtracted science one. This is because the estimation accuracies of the offset voltage and the gain fluctuation can be statistically

improved thanks to a number of the two types of reference pixels; the number of the onboard and outboard reference pixels for the current design of the OST transit spectrograph is approximately 3.6 x 10^6 (~ 1600 x 2000 + 400 x 1000), which is much larger than those of the reference pixels used in the previous observatories (e.g., Robberto et al. 2002).

We performed numerical simulations to investigate whether the calibration technique is valid for the transit observations. Figure D4 shows histograms of the science pixel values with and without calibration of the gain fluctuation by use of the two types of the reference pixels. The calibration technique successfully reduces the variation of the gain amplitude to Gaussian random noise and the residual noise is much smaller than the photon noise. As a result, because the photometric stability is ideally limited to the photon noise, the photometric accuracy is better as the integration time is longer (see Figure D5). We will investigate how much the gain fluctuation is calibrated with the two types of reference pixels, using a prototype of the OST transit spectrograph.

3.4. Final noise floor

Finally, we discuss the final noise floor for the OST transit spectrograph. As discussed in Section 3.1., the total amount of the noise floors is described by the root sum square of the photometric errors induced due to the telescope pointing jitter and detector gain fluctuation (see Equation (5)). In terms of the optical stability, because image movements on the intra- and inter-pixel sensitivity variations can be ignored thanks to a number of the science pixels, the slit loss and spatial filtering generated due to the field stop and finite optical elements limits the photometric stability. The photometric errors for the current design of the OST transit spectrograph are 3, 5, and 20 ppm for the telescope pointing jitters of 8, 10, and 20 mas, respectively. Note that the photometric error due to the slit loss is independent of the observing wavelength. On the other hand, the gain fluctuation generated in the detector and readout electronics is the fundamental limitation on the photometric accuracy of the OST transit spectrograph if there is not any calibration process. Focusing on a fact that there are a number of the reference pixels for the OST transit spectrograph, we developed a calibration technique for attenuation of the gain fluctuation in real time and found that the technique is valid for the transit observations. In this case, the final noise floor is mainly limited by the photon noise and slit loss variation. We will investigate how accurately the gain fluctuation can be calibrated with

the two types of reference pixels through an experiment with a prototype of the OST transit spectrograph.

References

Boss, A. P. Weinberger, A. J. Keiser, S. A. et al. 2017, accepted for publication in *Astron. J.* (arXiv: 1708.02200).

Deming, D. Seager, S. Winn, J. et al. 2009, *Pub. Astron. Soc. Pacific*, **121**, 952.

Gillon, M. Triaud, A. H. M. J. Demory, B.-O. et al. 2017, *Nature,* **542**, 456.

Greene, T. 2013, "Simulating Exoplanet Transit and Eclipse Observations with jwst," NASA technical reports server.

Itoh, S. Matsuo, T. Goda, S. et al. 2017, *Astron. J.*, **154**, 97.

Matsuo, T. Itoh, S. Shibai, H. et al. 2016, *Astrophys. J.* **823**, 139.

Robberto, M. Baggett, S. M. Hilbert, B. 2004, et al. *Proc. of SPIE*, **5499**, 15.

Proposal of ARIEL: The Atmospheric Remote-Sensing Infrared Exoplanet Large Survey, a candidate for the ESA M4 mission (http://sci.esa.int/future-missions-office/56560-phase-0-studies-completed-for-the-m4-cosmic-vision-candidate-missions/).

Appendix A. Pupil masks for reduction of slit loss

Satoshi Itoh

A1. Photometric error due to slit loss

Slit-loss variation with telescope pointing jitter, δO_{slit}, is one of the photometric-fluctuation sources in highly stable spectrophotometry. The slit-loss variation for one dimensional case can be estimated by

$$\delta O_{slit} \approx \left|\frac{d}{dx} PSF(x)|_{x=a}\right| \times \Delta\theta^2 , \tag{A1}$$

where a and $\Delta\theta$ are the slit radius and the pointing jitter normalized by λ/D, respectively. That is, δO_{slit} is proportional to the square of $\Delta\theta$, and the proportionality factor in Equation (A1) is the absolute value of the first-order differential coefficient of PSF at the edge of the slit. In the case of circular isotropic pupil function, the slit-loss variation can be similarly represented by

$$\delta O_{slit} \approx \frac{\pi a}{2} \left|\frac{\partial}{\partial r} PSF(r)|_{r=a}\right| \times \Delta\theta^2 . \tag{A2}$$

The field stop used for the OST transit spectrograph works similarly to the entrance slit in conventional spectrometers for reducing contamination from the background light sources such as stars, galaxies, and the thermal radiation from zodiacal light (Figure A1). Hence, the field-stop-loss variation induced by the telescope pointing jitter is one of the photometric-fluctuation sources for the OST transit spectrograph. The proportionality factor of the slit-loss variation corresponds to the case A in Figure A2.

A2. Pupil masks for high stable photometry

Pupil apodization mask can reduce the field-stop-loss variation, depressing the side lobe of the PSF, which corresponds to cases B-F in Figures A2 and A3. Especially, a new type of masks, called block-shaped mask, may be useful for reducing the field-stop-loss variation because these masks can make the PSF intensity variation in the vicinity of the edge of the field stop as close to zero as possible. They are designed such that the zeroth-, first-, second-, and third-order differential coefficients for the PSF at $x = a$ are exactly zero in analytical way and are represented by simple mathematical form (Figure A3). Under an assumption of a perfect optics, these block-shaped masks can achieve a slit-loss variation of 10 ppm for a nearly arbitrary field-stop radius even when the pointing jitter is approximately 0.7λ/D. They can also achieve a slit-loss variation of 1 ppm even at a

pointing jitter of approximately 0.5λ/D. Note that the block-shaped masks used for polychromatic light require the field stop with radius proportional to the wavelength of light.

A3. Effect of optical aberration on slit-loss variation

In real observations, we have to consider an impact of optical aberration on ideal PSF shapes. To mathematically describe the degradation of the ideal PSF shapes, we introduce the following model as an expression for a power-spectral density (PSD) of high-order phase aberration:

$$PSD(k) = \frac{3\sqrt{3}}{4\pi^2 k_0^2} \frac{1-S}{1+\left(\frac{k}{k_0}\right)^3}, \tag{A3}$$

where S is the Strehl ratio, k is the absolute value of the wave number of the phase fluctuation, and k_0=*10* cycle/pupil. The unit of k is cycle/pupil and the unit of $PSD(k)$ is radian^2/(cycle/pupil)^2. Given that the phase aberration is sufficiently less than unit radian, the impact of the phase aberration on the PSF can be estimated as follows:

$$\begin{aligned} PSF_\psi(r) &= PSF_0(r) + PSF_0(r) * PSD(r) \\ &\approx PSF_0(r) + \pi\tau PSD(r) \end{aligned} \tag{A4}$$

where $*$ is a two-dimensional convolution operator with respect to x and y, which satisfy $\mathrm{r} = \sqrt{x^2+y^2}$, $PSF_\psi(r)$ and $PSF_0(r)$ represent the PSF with and without the phase aberration, respectively, and τ is energy transmittance of a mask. The PSF degradation due to the optical aberration depends on the mask profiles only by its transmissivity, τ; the impact of high-order aberration is almost unchanged by the mask type. Hence, $\delta O_{slit}/\Delta\theta^2$ is limited by

$$\frac{\delta O_{slit}}{\Delta\theta^2} = \frac{\pi a}{2}\left|\frac{\partial}{\partial r} PSF_\psi(r)|_{r=a}\right| \le \frac{\pi a}{2}\left|\frac{\partial}{\partial r} PSF_0(r)|_{r=a}\right| + \frac{\tau\pi^2 a}{2}\left|\frac{\partial}{\partial r} PSD(r)|_{r=a}\right|. \tag{A5}$$

The second term represents the degradation of the photometric stability due to wave-front-aberration and can be estimated by

$$\frac{\tau\pi^2 a}{2}\left|\frac{\partial}{\partial r} PSD(r)|_{r=a}\right| = \frac{9\sqrt{3}\tau a}{8000} \frac{1-S}{\left(1+\left(\frac{a}{10}\right)^3\right)^2}. \tag{A6}$$

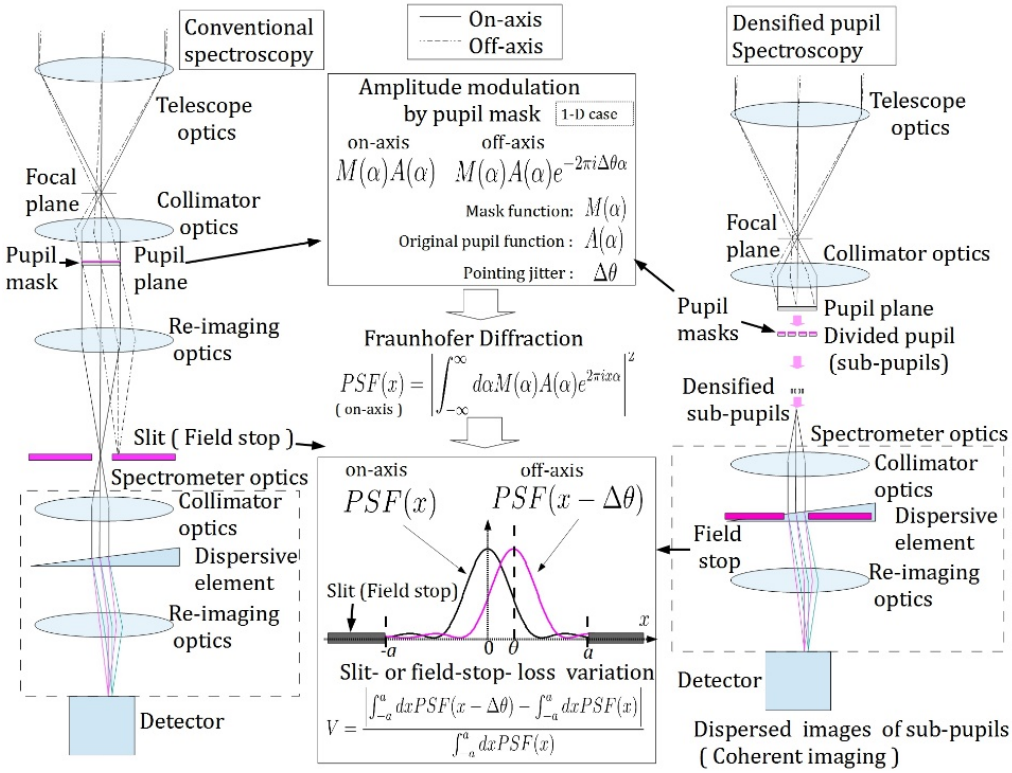

Figure A1. Schematic of the layout of the pupil mask and field stop for a conventional spectrograph (left) and the OST transit spectrograph (right). Note that α is normalized by the pupil radius. $\Delta\theta$, a, and x are normalized by λ/D.

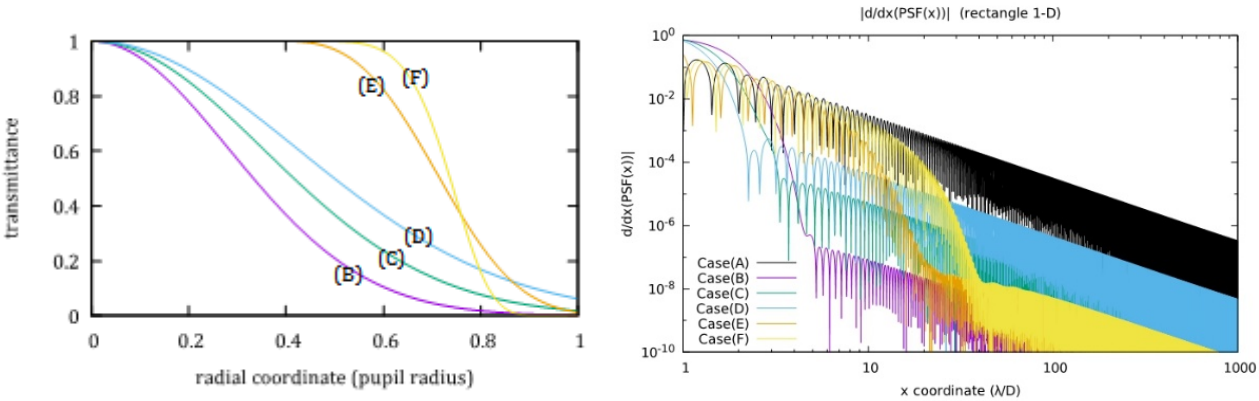

Figure A2. Amplitude transmittances of masks as a function of pupil radius (left) and $\left|\frac{d}{dx}PSF(x)|_{x=a}\right|$ for 1-D rectangular apodizing masks (right). We assume that no optical aberration exists in this simulation.

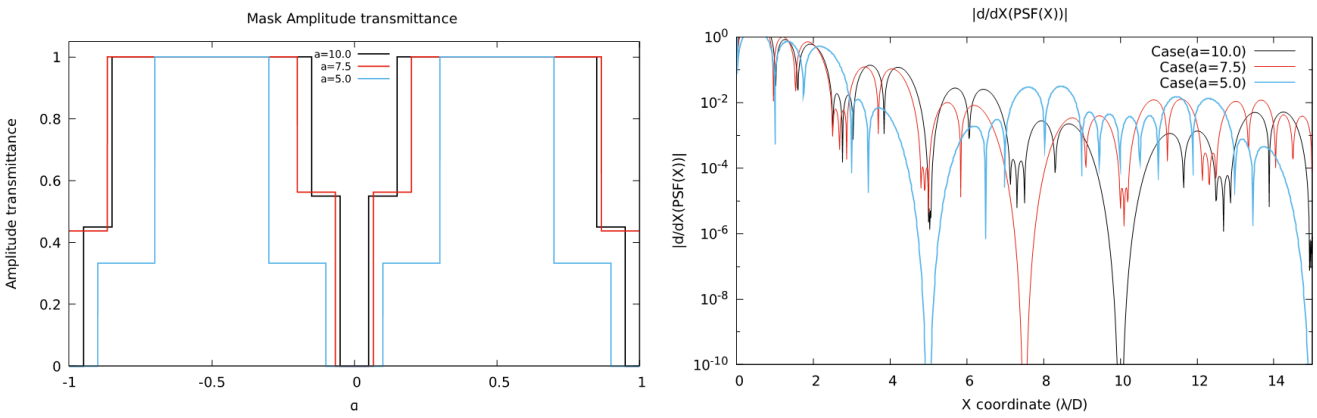

Figure A3. Pupil functions of 1-D block-shaped masks (left) and $\left|\frac{d}{dx}PSF(x)|_{x=a}\right|$ for 1-D block-shaped masks (right).

Appendix B. Analysis of wavefront propagation

Masayuki Ido

B.1. Wavefront propagation

In this section, we introduce the results of wavefront analysis for the current OST transit spectrograph with the VirtualLab software, which can perform various optical simulations including Fresnel diffraction and spectrum of plane wave (SPW). The spectrum of plane wave is one of the techniques for modelling the propagation of a wave field at the same level as the electromagnetic field analysis without increasing the computational cost. Figure B1 shows an optical model used for calculation of the wavefront propagation. Note that the grating put on the focal plane is not included because only the impact of spatial filtering due to finite optical elements is evaluated. The wavelength used for this simulation is fixed to 20μm. Figure B2 shows the intensity distributions of the densified pupil and pupil on the detector. While the densified pupil is tidily reimaged, the pupil image on the detector plane is slightly disturbed in a horizontal direction. This is because the spatial filtering occurred in the spectrograph is much larger than that in the pupil remapping and densification part. However, based on the number of the periodic patterns observed on the detector plane, an effect of the spatial filtering in the spectrograph is almost equal to that due to a field stop with a diameter of $12\lambda/D$ put on the focal plane; the spatial filtering induced by the optical elements does not largely contribute to the final noise floor.

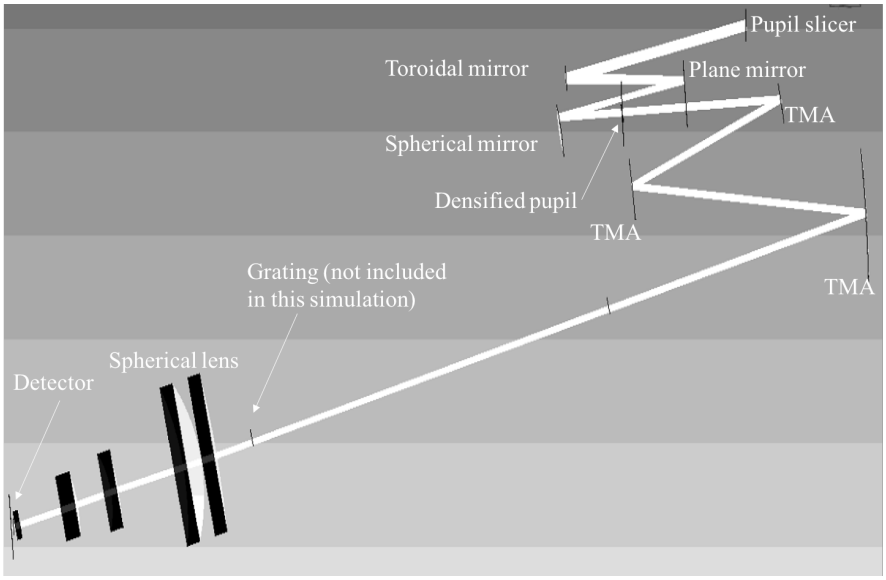

Figure B1. Optical model used for wavefront analysis. The dichroic mirror and grating are not included in this model.

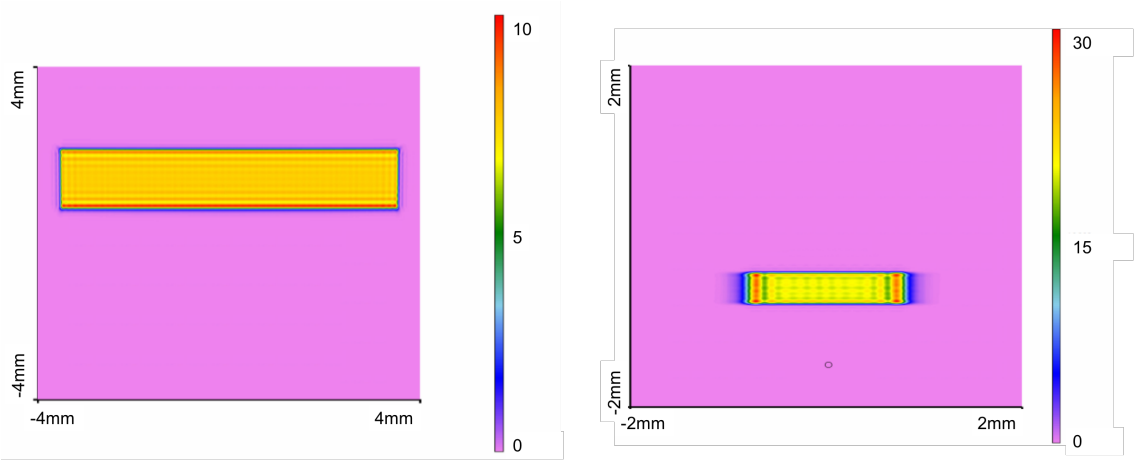

Figure B2. Intensity distributions of the densified pupil (left) and pupil on the detector plane (right). The horizontal and vertical axes correspond to the spatial and spectral directions, respectively.

B.2. Image movement

Next, we calculated the pupil displacement on the detector induced by the telescope pointing jitter. Figure B3 shows the image movements on the detector plane at 20μm for various magnitudes of the pointing jitter. The image displacement is less than 0.15 pixel when the pointing jitter is smaller than 0.1 λ/D, assuming that the detector pixel size is 30μm.

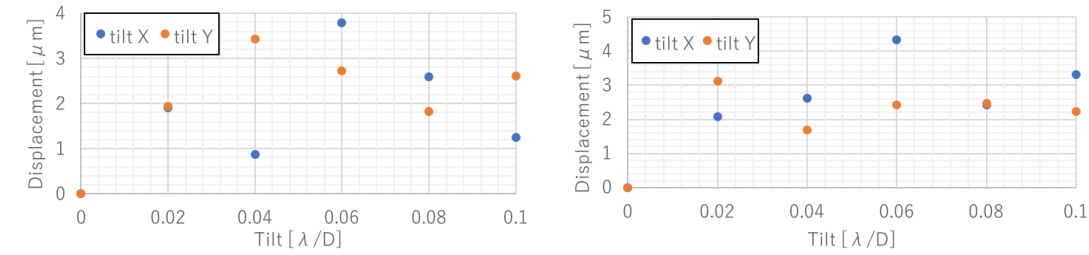

Figure B3. Displacements of pupil image on the detector plane induced by various magnitudes of tilt.

Appendix C. Modelling of detector and readout electronics

Taro Matsuo

In this section, we formulate the detailed models of the science and reference pixels to introduce a method for calibration of the fluctuation of detector gain with the two types of reference pixels (see Appendix D). Figures C1 shows a conceptual diagram of the detector and its readout electronics applied in the OST transit spectrograph. The parameters used in this section are explained in Appendix E. To mathematically describe the fluctuations and random noises generated in the detector and readout electronics, we assume that the optical transmissivity does not change over time in this section.

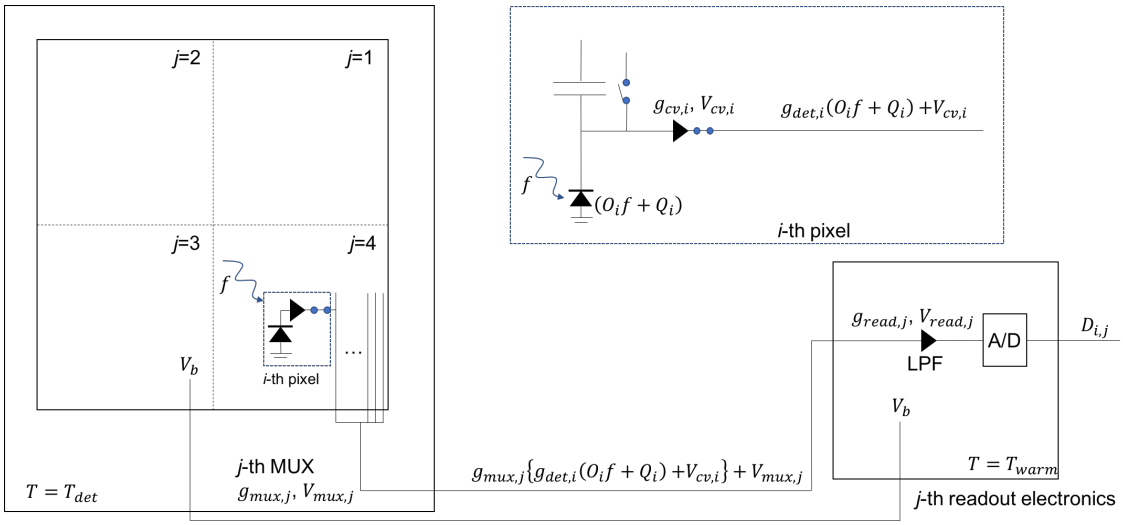

Figure C1. Conceptual diagram of detector and its readout electronics.

C1. Science pixel value

When no fluctuation and random noise exists in the detector and readout electronics (i.e., ideal case), the signal value of the *i*-th science pixel with the *j*-th multiplexer (MUX) and readout electronics is

$$D_{sci0,i,j}(t) = \langle g_{read,j}\rangle_t\left[\langle g_{mux,j}\rangle_t\left[\langle g_{det,i}\rangle_t\{\langle O_i\rangle_t f + Q_i\} + V_{cv,i}\right] + V_{mux,j}\right] + V_{read,j}, \quad \text{(C1)}$$

where $A(B)$ means that parameter A has B dependence and $\langle A\rangle_t$ shows the average parameter A over time. In reality, since the temperatures of the detector and readout electronics fluctuate, some of the parameters in Equation (C1) such as O_i, $g_{read,j}$, $g_{mux,j}$, $g_{det,i}$, and Q_i change over time. There are also random noises accompanied with incident flux, readout electronics, and digitalization. The *i*-th science pixel value

with the j-th MUX and readout electronics can be decomposed into superposition of the average value (DC component), fluctuation term, and random noise:

$$D_{sci,i,j}(t) = \langle D_{sci,i,j}\rangle_t + \delta D_{sci,i,j}(t) + \sigma_{sci,i,j}. \quad \text{(C2)}$$

The first term on the right hand side in Equation (C2) equals to the average value of $D_{sci0,i,j}$:

$$\begin{aligned}\langle D_{sci,i,j}\rangle_t &= \langle g_{read,j}\left[g_{mux,j}\left\{g_{det,i}(O_i f + Q_i) + V_{cv,i}\right\} + V_{mux,j}\right] + V_{read,j}\rangle_t \\ &= \langle g_{read,j}\rangle_t\langle g_{mux,j}\rangle_t\langle g_{det,i}\rangle_t(\langle O_i\rangle_t\langle f\rangle_t + \langle Q_i\rangle_t) + \langle g_{read,j}g_{mux,j}V_{cv,i}\rangle_t \\ &\quad + \langle g_{read,j}V_{mux,j}\rangle_t + V_{read,j}, \end{aligned} \quad \text{(C3)}$$

where we assume that each parameter is independent of each other. The sum of the second, third, and fourth terms in Equation (C3) corresponds to the average offset component over time attached to the i-th pixel with the j-th MUX and readout electronics,

$$\langle V_{i,j}\rangle_t = \langle g_{read,j}g_{mux,j}V_{cv,i}\rangle_t + \langle g_{read,j}V_{mux,j}\rangle_t + V_{read,j}. \quad \text{(C4)}$$

Given that more than second-order fluctuations are ignored and the variation of the dark current, δQ_i, is much smaller than the transit signal, δf, the fluctuation term in Equation (C2), $\delta D_{sci,i,j}(t)$, becomes

$$\begin{aligned}\delta D_{sci,i,j}(t) \approx\ & \langle g_{read,j}\rangle_t\langle g_{mux,j}\rangle_t\langle g_{det,i}\rangle_t\langle O_i\rangle_t\delta f \\ &+\langle g_{mux,j}\rangle_t\left[\left\{\langle g_{det,i}\rangle_t(\langle O_i\rangle_t\langle f\rangle_t + \langle Q_i\rangle_t) + V_{cv,i}\right\} + V_{mux,i}\right]\delta g_{read,j} \\ &+\langle g_{read,j}\rangle_t\langle g_{det,i}\rangle_t\left\{(\langle O_i\rangle_t\langle f\rangle_t + \langle Q_i\rangle_t) + V_{cv,i}\right\}\delta g_{mux,j} \\ &+\langle g_{read,j}\rangle_t\langle g_{mux,j}\rangle_t(\langle O_i\rangle_t\langle f\rangle_t + \langle Q_i\rangle_t)\delta g_{det,i}. \end{aligned} \quad \text{(C5)}$$

The fluctuation of the science data is mainly composed of the following three terms. The first is the transit signal

$$\delta D_{signal,i,j}(t) \approx \langle g_{read,j}\rangle_t\langle g_{mux,j}\rangle_t\langle g_{det,i}\rangle_t\langle O_i\rangle_t\delta f. \quad \text{(C6)}$$

The second is the variation of transit signal induced by the gain fluctuation:

$$\begin{aligned}\delta g_{i,j} = \langle O_i\rangle_t\langle f\rangle_t(&\langle g_{mux,i}\rangle_t\langle g_{det,i}\rangle_t\delta g_{read,j} + \langle g_{read,j}\rangle_t\langle g_{det,i}\rangle_t\delta g_{mux,j} \\ &+\langle g_{read,j}\rangle_t\langle g_{mux,j}\rangle_t\delta g_{det,i}). \end{aligned} \quad \text{(C7)}$$

The third is the variation of offset voltage occurred due to the gain fluctuation

$$\delta V_{i,j} = \langle g_{mux,i}\rangle_t\left(\langle g_{det,i}\rangle_t V_{cv,i} + V_{mux,j}\right)\delta g_{read,j} + \langle g_{read,j}\rangle_t\langle g_{det,i}\rangle_t V_{cv,i}\delta g_{mux,j}. \quad \text{(C8)}$$

The second term is the fundamental limitation on the general transit observations because the transit signal cannot be separated from the gain fluctuation occurred in the detector and readout electronics. On the other hand, the contribution of the offset voltage to the science pixels, $\langle V_{i,j}\rangle_t + \delta V_{i,j}$, is potentially estimated from the outboard reference pixels,

in which only the offset voltage is generated. The random noise is composed of σ_{photon}, σ_{dark}, and σ_{read}. Because the three random noises are statistically independent, the random noise included in the *i*-th science pixel value with the *j*-th readout electronics can be written as

$$\sigma_{sci,i,j} \approx \sqrt{\sigma_{photon,i}^2 + \sigma_{dark,i}^2 + \sigma_{read,j}^2}, \tag{C9}$$

where noise generated in an analog-to-digital conversion is included in the readout noise.

C2. Two types of reference pixels

As introduced in Section 2.4, there are two types of reference pixels: onboard and outboard reference pixels. Both of them are shielded from any thermal radiation with the cold-photon shield mask (blue-colored region represented in Figure 4). In addition, there is no connection between the Si:As focal plane array and the Si ROIC in the latter. As a result, while the dark current produced by leakage in the photoconductor and the offset voltage are sources in the onboard reference pixels, only the offset voltage is generated in the outboard reference pixels.

C2.1. Onboard reference pixel

In analogy with formulation of the science pixel value, the onboard reference pixel value can be written as the sum of the average, fluctuation over time, and random noise terms:

$$D_{onref,i,j}(t) = \langle D_{onref,i.j}\rangle_t + \delta D_{onref,i,j}(t) + \sigma_{onref,i,j}. \tag{C10}$$

The difference between the science and onboard reference pixel values is whether the electric charge produced by the incident flux exists or not. Therefore, the onboard reference pixel value averaged over time is

$$\begin{aligned}\langle D_{onref,i,j}\rangle_t &= \langle g_{read,j}\left[g_{mux,j}\left[g_{det,i}Q_i + V_{cv,i}\right] + V_{mux,j}\right] + V_{read,j}\rangle_t \\ &= \langle g_{read,j}g_{mux,j}g_{det,i}Q_i\rangle_t + \langle g_{read,j}g_{mux,j}V_{cv,i}\rangle_t \\ &\quad + \langle g_{read,j}V_{mux,i}\rangle_t + \langle V_{read,j}\rangle_t,\end{aligned} \tag{C11}$$

the fluctuation term is

$$\begin{aligned}\delta D_{onref,i,j}(t) \approx &\left[\langle g_{mux,j}\rangle_t\left\{\langle g_{det,i}\rangle_t\langle Q_i\rangle_t + V_{cv,i}\right\} + V_{mux,j}\right]\delta g_{read,j} \\ &+ \langle g_{read,j}\rangle_t\langle g_{det,i}\rangle_t\left\{\langle Q_i\rangle_t + V_{cv,i}\right\}\delta g_{mux,j} \\ &+ \langle g_{read,j}\rangle_t\langle g_{mux,j}\rangle_t\langle Q_i\rangle_t\delta g_{det,i},\end{aligned} \tag{C12}$$

and the random noise is

$$\sigma_{onref,i,j} \approx \sqrt{\sigma_{dark,i}^2 + \sigma_{read,j}^2}. \quad \text{(C13)}$$

C2.2. Outboard reference pixel

Similarly, the value of the *i*-th outboard reference pixel is written as the superposition of the average value, fluctuation term, and random noise:

$$D_{outref,i,j}(t) = \langle D_{outref,i.j}\rangle_t + \delta D_{outref,i,j}(t) + \sigma_{outref,i,j}. \quad \text{(C14)}$$

Because only the offset voltage is generated in the outboard reference pixels, the outboard reference pixel value is the product of the offset voltage and gain amplitudes. As a result, each term in Equation (C13) is described as follows:

$$\begin{aligned}\langle D_{outref,i,j}\rangle_t &= \langle g_{read,j}\left[g_{mux,j}V_{cv,i} + V_{mux,j}\right] + V_{read,j}\rangle_t \\ &= \langle g_{read,j}g_{mux,j}V_{cv,i}\rangle_t + \langle g_{read,j}V_{mux,i}\rangle_t + \langle V_{read,j}\rangle_t, \quad \text{(C15)}\end{aligned}$$

$$\delta D_{outref,i,j}(t) \approx \left[\langle g_{mux,j}\rangle_t V_{cv,i} + V_{mux,j}\right]\delta g_{read,j} + \langle g_{read,j}\rangle_t\langle g_{det,i}\rangle_t V_{cv,i}\delta g_{mux,j}, \quad \text{(C16)}$$

and

$$\sigma_{outref,i,j} \approx \sigma_{read,j}. \quad \text{(C17)}$$

Appendix D. Calibration of detector gain with reference pixels

Shohei Goda

In this section, we explain a method for calibration of the gain fluctuation, by which the transit signals are affected, and evaluate the performance of the calibration method through numerical simulations. The symbols used in this section are compiled in Appendix E2.

D1. Method

We mathematically describe the process for calibrating the gain fluctuation by use of the two types of reference pixels, onboard and outboard reference pixels. The value of the outboard reference pixel on the i-th pixel with the j-th multiplexer and readout electronics is

$$\begin{aligned} D_{outref i,j}(t) &= g_{read,j}(t)g_{mux,j}(t)V_{cv,i} + g_{read,j}(t)V_{mux,j} + V_{read,j} \\ &= \langle g_{read,j}\rangle_t \langle g_{mux,j}\rangle_t V_{cv,i} + \langle g_{read,j}\rangle_t V_{mux,j} + V_{read,j} \\ &\quad + \left(\langle g_{mux,j}\rangle_t V_{cv,i} + V_{mux,j}\right)\delta g_{read,j}(t) + \langle g_{read,j}\rangle_t V_{cv,i}\delta g_{mux,j}(t) \\ &\quad + \sigma_{read,i,j}. \end{aligned} \tag{D1}$$

Because the values of the outboard reference pixels are measured at the same time, we can remove the component induced by the offset voltage from the science data through subtraction of Equation (D1) from Equation (C2):

$$D'_{sci,i,j}(t) = D_{sci,i,j}(t) - D_{outref,i,j}(t) = \langle D'_{sci,i,j}\rangle_t + \delta D'_{sci,i,j}(t) + \sigma'_{sci,i,j}. \tag{D2}$$

The term on the right-hand side in Equation (D2) equals to superposition of the average value, fluctuation, and random noise. Each term is mathematically described as follows:

$$\langle D'_{sci,i,j}\rangle_t = \langle g_{read,j}\rangle_t \langle g_{mux,j}\rangle_t \langle g_{det,i}\rangle_t (\langle O_i\rangle_t \langle f\rangle_t + \langle Q_i\rangle_t), \tag{D3}$$

$$\begin{aligned} \delta D'_{sci,i,j}(t) &= \langle g_{read,j}\rangle_t \langle g_{mux,j}\rangle_t \langle g_{det,i}\rangle_t \langle O_i\rangle_t \delta f_i(t) \\ &\quad + \langle g_{mux,j}\rangle_t \langle g_{det,i}\rangle_t (\langle O_i\rangle_t \langle f_i\rangle_t + \langle Q_i\rangle_t)\delta g_{read,j}(t) \\ &\quad + \langle g_{read,j}\rangle_t \langle g_{det,i}\rangle_t (\langle O_i\rangle_t \langle f_i\rangle_t + \langle Q_i\rangle_t)\delta g_{mux,j}(t) \\ &\quad + \langle g_{read,j}\rangle_t \langle g_{mux,j}\rangle_t (\langle O_i\rangle_t \langle f_i\rangle_t + \langle Q_i\rangle_t)\delta g_{det,i}(t) \\ &= \langle g_{read,j}\rangle_t \langle g_{mux,j}\rangle_t \langle g_{det,i}\rangle_t \langle O_i\rangle_t \delta f_i(t) + (\langle O_i\rangle_t \langle f_i\rangle_t + \langle Q_i\rangle_t) \\ &\quad \times \left\{\langle g_{mux,j}\rangle_t \langle g_{det,i}\rangle_t \delta g_{read,j}(t) + \langle g_{read,j}\rangle_t \langle g_{det,i}\rangle_t \delta g_{mux,j}(t) + \right. \\ &\quad \left. \langle g_{read,j}\rangle_t \langle g_{mux,j}\rangle_t \delta g_{det,i}(t)\right\}, \end{aligned} \tag{D4}$$

and

$$\sigma'_{\mathrm{sci,i,j}} = \sqrt{\sigma^2_{sci,i,j} + \sigma^2_{read,i,j}}. \tag{D5}$$

Similarly, we can remove the offset component for the onboard reference pixels:

$$D'_{onref,i,j}(t) = D_{onref,i,j}(t) - D_{outrefi,j}(t) = \left\langle D'_{onref,i,j} \right\rangle_t + \delta D'_{onref,i,j}(t) + \sigma'_{onref,i,j}, \tag{D6}$$

where the average term is

$$\left\langle D'_{onref,i,j} \right\rangle_t = \left\langle g_{read,j} \right\rangle_t \left\langle g_{mux,j} \right\rangle_t \left\langle g_{det,i} \right\rangle_t \langle Q_i \rangle_t, \tag{D7}$$

the fluctuation term is

$$\begin{aligned} \delta D'_{onref,i,j}(t) = {} & \left\langle g_{mux,j} \right\rangle_t \left\langle g_{det,i} \right\rangle_t \langle Q_i \rangle_t \delta g_{read,j}(t) \\ & + \left\langle g_{read,j} \right\rangle_t \left\langle g_{det,i} \right\rangle_t \langle Q_i \rangle_t \delta g_{mux,j}(t) \\ & + \left\langle g_{read,j} \right\rangle_t \left\langle g_{mux,j} \right\rangle_t \langle Q_i \rangle_t \delta g_{det,i}(t) \\ = {} & \langle Q_i \rangle_t \left\{ \left\langle g_{mux,j} \right\rangle_t \left\langle g_{det,i} \right\rangle_t \delta g_{read,j}(t) + \left\langle g_{read,j} \right\rangle_t \left\langle g_{det,i} \right\rangle_t \delta g_{mux,j}(t) + \right. \\ & \left. \left\langle g_{read,j} \right\rangle_t \left\langle g_{mux,j} \right\rangle_t \delta g_{det,i}(t) \right\}, \end{aligned} \tag{D8}$$

and the random noise is

$$\sigma'_{onref,i,j} = \sqrt{\sigma^2_{onref,i,j} + \sigma^2_{read,i,j}}. \tag{D9}$$

Hence, we can calibrate the gain fluctuation of the science pixels with the subtracted onboard reference pixels. The subtraction of the subtracted-onboard-reference-pixel-value from the science data is

$$\begin{aligned} D_{sub,i,j}(t) = {} & D'_{sci,i,j}(t) - \left(D'_{onref,i,j} - \left\langle D'_{onref,i,j} \right\rangle_t \right) \times \frac{\left\langle D'_{sci,i,j} \right\rangle_t}{\left\langle D'_{onref,i,j} \right\rangle_t} - \left\langle D'_{onref,i,j} \right\rangle_t \\ = {} & \left\langle g_{read,j} \right\rangle_t \left\langle g_{mux,j} \right\rangle_t \left\langle g_{det,i} \right\rangle_t \langle O_i \rangle_t \langle f_i \rangle_t \\ & + \left\langle g_{read,j} \right\rangle_t \left\langle g_{mux,j} \right\rangle_t \left\langle g_{det,i} \right\rangle_t \langle O_i \rangle_t \delta f_i(t) + \sigma_{sub,i,j}. \end{aligned} \tag{D10}$$

This process does not subtract only the gain fluctuation but also the dark current from the science data. The last term on the right-hand side in Equation (D10) equals to

$$\sigma_{sub,i,j} = \sqrt{\sigma'^2_{sci,i,j} + \left(\frac{\left\langle D'_{sci,i,j} \right\rangle_t}{\left\langle D'_{onref,i,j} \right\rangle_t} \sigma'_{onref,i,j} \right)^2}. \tag{D11}$$

We get the summation value through the following calculation:

$$D_{sub,bin}(t) = \Sigma_i^{n_{sci}} D_{sub,i,j}(t)$$
$$= n_{sci}\{\langle g_{com}\rangle_t \langle O\rangle_t \langle f\rangle_t + \langle g_{com}\rangle_t \langle O\rangle_t \delta f(t)\} + \sqrt{n_{sci}}\sigma_{sub}. \quad \text{(D12)}$$

When the summation value is normalized to one, the above equation becomes

$$\frac{D_{sub,bin}(t)}{\langle D_{sub,bin}\rangle_t} = 1 + \frac{\delta f(t)}{\langle f\rangle_t} + \sigma_{sub,bin}. \quad \text{(D13)}$$

The last term on the right-hand side in Equation (D13) equals to

$$\sigma_{sub,bin} = \frac{\sigma_{sub}}{\langle g_{com}\rangle_t \langle O\rangle_t \langle f\rangle_t \sqrt{n_{sci}}}. \quad \text{(D14)}$$

Only the electric charges produced by the incident flux and random noise remain through the above calibration process. As a result, the longer the observation time is, the better the photometric accuracy is.

Figure D1 shows the flowchart of the calculation method. In this simulation, although the spectral resolutions for the OST transit spectrograph are set to 100, 100, and 300 for the three wavelength ranges of 6-11μm, 11-18μm, and 18-25μm, respectively, we performed binning of the science data to suppress the photon noise. Note that the final spectral resolution for all the simulations is fixed to 20.

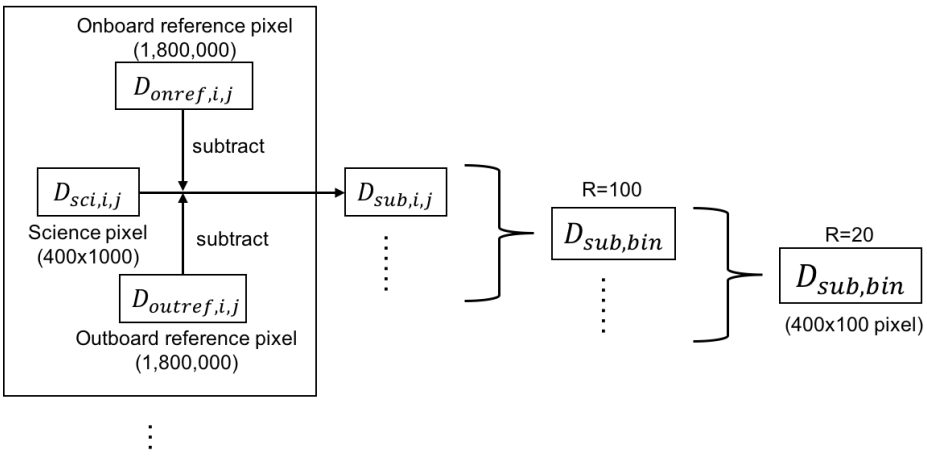

Figure D1. Flowchart of calculation method.

D2. Setup

We take the Trrappist-1 system as an example of the transit observation with OST to evaluate the performance of the calibration technique introduced above. The parameters of the host star and its planet e in the Trappist-1 system are referred to the previous studies

(Gillon et al. 2017; Boss, et al., 2017). Based on the parameters compiled in Tables D1, D2, and D3, we generated the transit curves of the Trappist-1 system. We also made the long-term variations of the onboard and outboard reference pixels according to Equation (D6).

Table D1. Characteristics of the Trappist-1 system

Items	Value
Star	**TRAPPIST-1=2MASS J23062928-0502285**
Distance (pc)	12.56 ± 0.12
Radius ($R_{\odot}$)	0.117 ± 0.0036
Effective temperature (K)	2559 ± 50
Planet	**e**
Period (days)	$6.099615 \pm 0.11\times10^{-4}$
Inclination (°)	$89.86^{+0.10}_{-0.12}$
Semi-major axis (10^{-3}AU)	$28.17^{+0.83}_{-0.87}$
Radius (R_{Earth})	0.918 ± 0.039
Equilibrium temperature (K)	251.3 ± 4.9

Table D2. Specifications of the OST and its transit spectrograph

Items	Values
OST	**-**
Primary mirror diameter (cm)	930
Transit spectrograph	**-**
Number of science pixels	400,000
Number of onboard reference pixels	1,800,000
Number of outboard reference pixels	1,800,000
Transmittance inq. QE (%)	30
Range of wavelength (μm)	6~25
Spectral resolution ($\lambda/\Delta\lambda$)	100 (6~18μm), 300 (18~25μm)
Exposure time at one time (sec)	120

Table D3. Assumptions of model curves

Items	Values
Photon noise	No (Tests 1 and 2), Yes (Test 3)
Limb darkening	*Linear
**Peak-to-peak of gain fluctuation (ppm)	500
Dark current (electron/sec)	0.2
Readout noise (electron/time)	14

*In this simulation, we used the values from 0.01 to 0.26 as limb darkening constants in the wavelength range of 6-25μm that are extrapolated from those in near infrared.

**The gain fluctuation depends on the instability of the bias voltage induced by change of the temperatures of the detector and readout electronics and is in inverse proportion to frequency. In this simulation, we summed up sine curves that had different frequency such that the peak-to-peak amplitude of the summation curve is 500ppm.

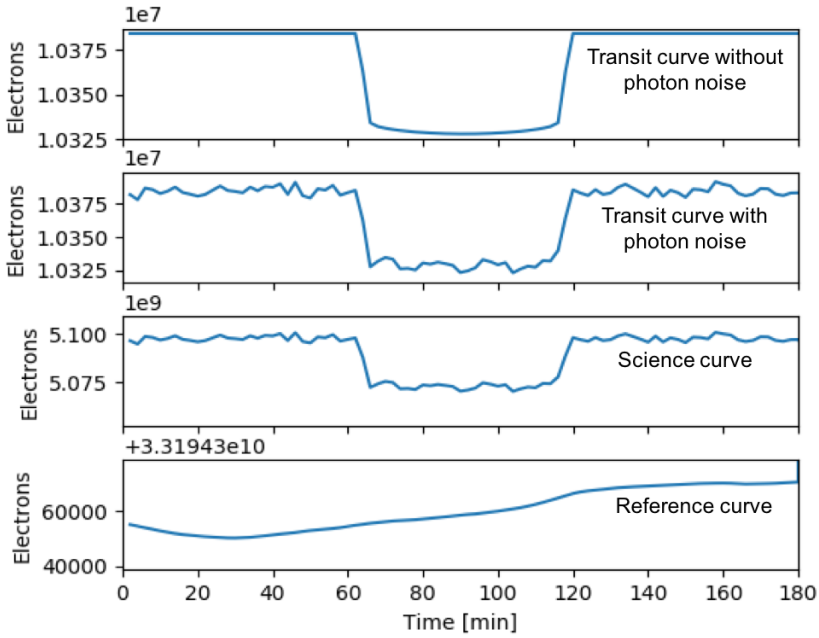

Figure D2. Transit light curve of primary eclipse without photon noise (top), transit curve with photon noise (second row), science data (third row), and onboard reference data (bottom).

D4. Evaluations

We validate the effectiveness of the method for calibration of the gain fluctuation with the two types of reference pixels through the following three tests. The first is to investigate whether we can calibrate the gain fluctuation for data, which is product of a constant signal and the gain fluctuation. The second is to confirm whether the calibration technique is valid for a transit curve without photon noise. The third is to study whether we can remove the gain fluctuation for a transit curve with photon noise and to evaluate the photometric accuracy over the entire wavelength range of the OST transit spectrograph.

D4.1. Constant signal with gain fluctuation

We first show the science data before and after applying the calibration technique to the science data in Figure D3 and also introduce the histograms of the model signals before and after the calibration in Figure D4. We found that the distribution of the science data after the calibration is approximately a Gaussian function; the gain fluctuation can be reduced to the random noise. Thus, we successfully calibrated the gain fluctuation with the reference pixels for the constant signal.

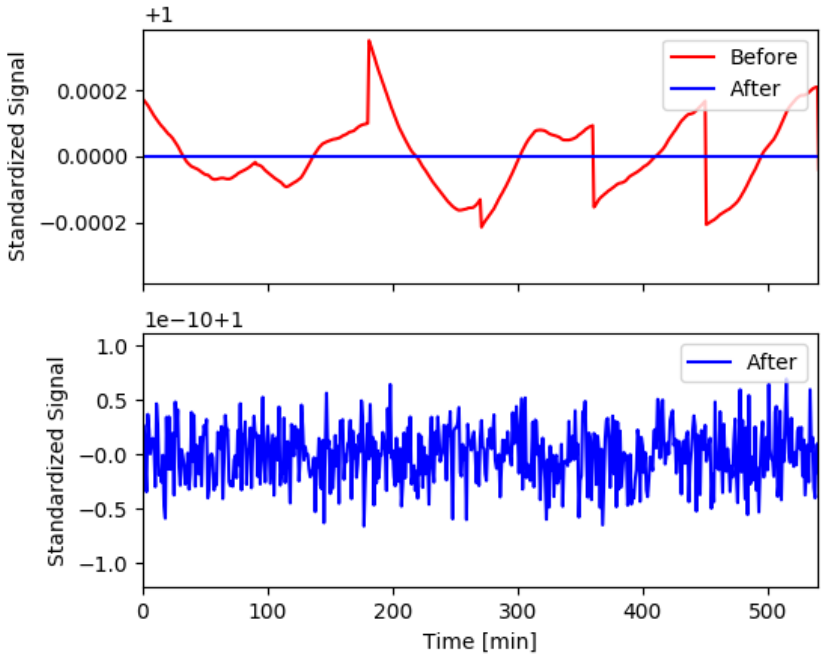

Figure D3. Model signals before and after the calibration.

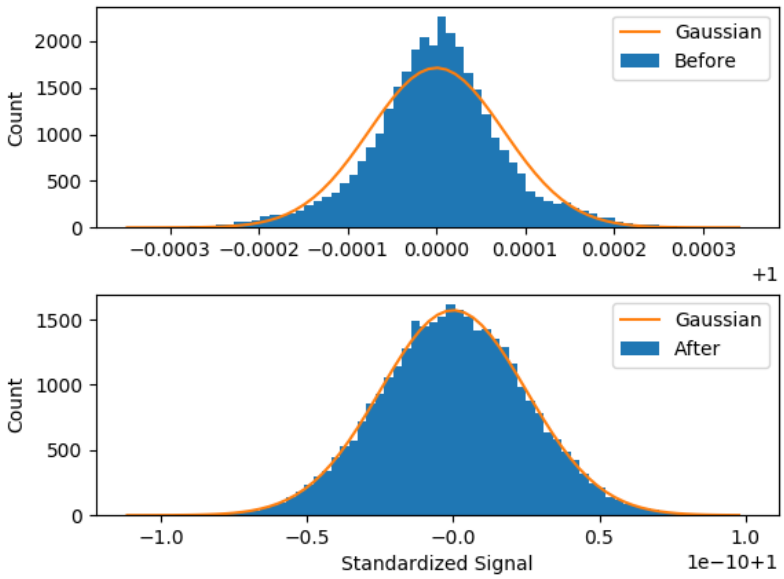

Figure D4. Histograms of model signals before (top) and after (bottom) the calibration.

D4.2. Transit light curve with gain fluctuation

Next, the results of the second test are discussed. We changed the input signal used in the first test to transit light curves occurred in the primary eclipse and combined the curves into one transit light curve. We evaluated a difference between the original depth (input signal) and one estimated from the transit curve after the calibration (result) and then derived the calibration accuracy of the gain fluctuation before and after the calibration as a function of the number of transits. In this evaluation, we normalized the light curve continuum to one. Note that the rms measurement error of offset value without any calibration technique is expected to be 300ppm. The top and bottom panels shown in Figure D5 are the photometric accuracies for the science data before and after applying the calibration, respectively. While the photometric accuracy for the light curve without any calibration method is not much improved even with many transit observations, the photometric error of the data reduced through the calibration can be more minimized as the number of transits. The photometric accuracy of the calibrated data is approximately proportional to the root of the number of transits.

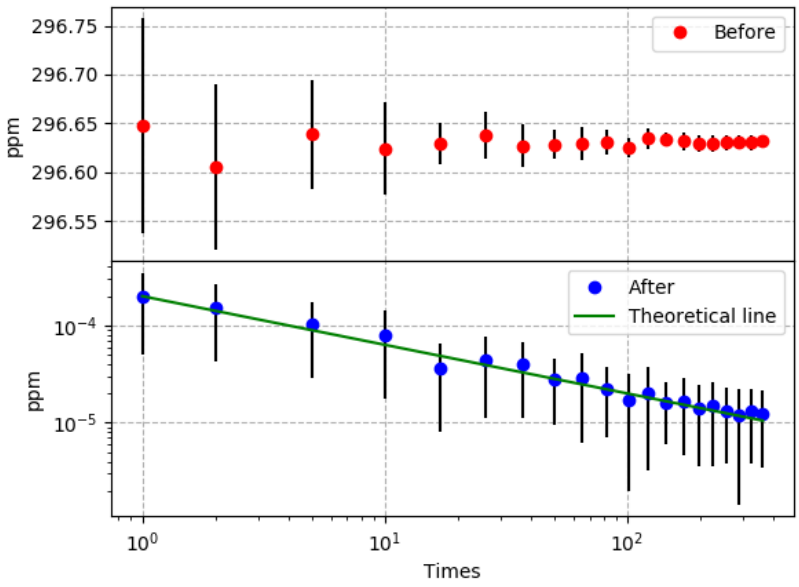

Figure D5. Evaluations of photometric accuracies with (bottom) and without (top) the calibration technique for transit light curves without photon noise.

D4.3. Transit light curve with gain fluctuation and photon noise

Finally, we show the results for the transit light curve with both of the gain fluctuation and photon noise. We generated the model curves of the Trappist-1 system for both of the transmission and secondary eclipse as a function of the wavelength and evaluated the performance of the calibration method in the same fashion as the second test. Figures D6 and D7 show comparisons of the performance with the requirements for observations of the transmission spectroscopy and secondary eclipse of Trappist-1e. Note that the scale height for the transmission spectroscopy is set to 10 km. As shown in Figures D6 and D7, the photometric accuracy at the longer wavelength is worse than the shorter one because the photon noise more limits the photometric accuracy in the longer wavelength range. In addition, the photometric accuracy becomes better with increasing the number of transits, meaning that the science data reduced through the calibration technique leaves only the transit signal and random noise. Comparing the acquired photometric accuracy to the requirements for observations of the primary transmission and secondary eclipse, we concluded that, while the shorter wavelength range is suited for observation of the primary transmission, the longer one is appropriate to the secondary eclipse.

Thus, we found that the calibration technique is valid for the gain fluctuations given in the above tests and enhances the photometric accuracy to the ideal photon noise limit under the assumption that the fluctuation of the optical system is ignored.

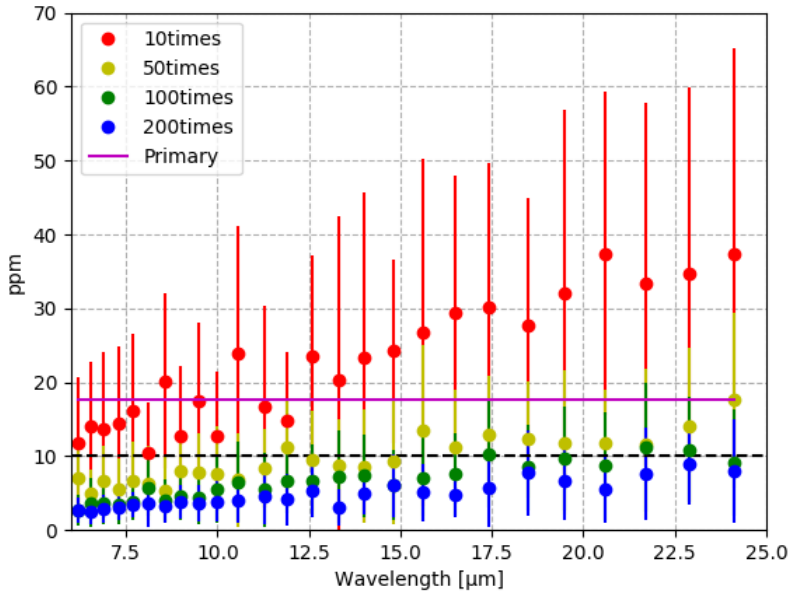

Figure D6. Evaluation of the calibration technique for primary transmission data.

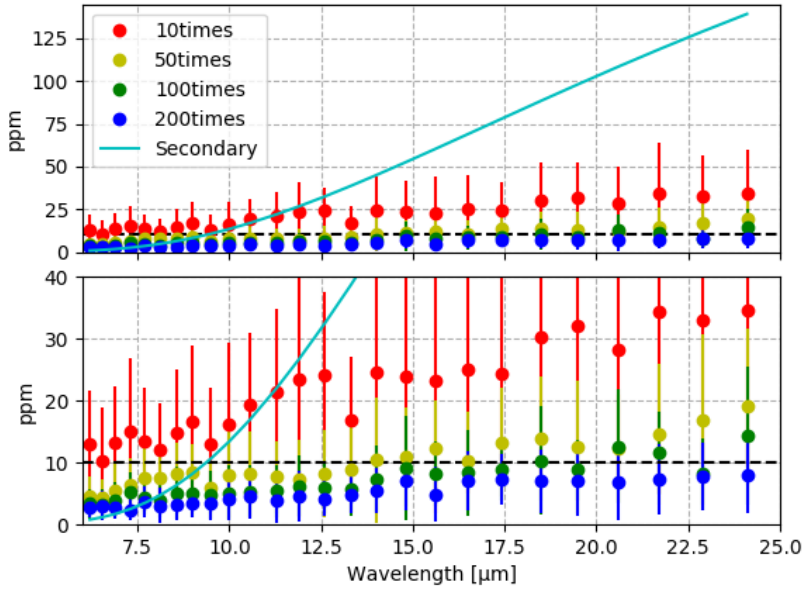

Figure D7. Evaluation of the calibration technique for secondary eclipse data.

Appendix E. Assumptions and Parameters

E1. Assumptions

The assumptions used for evaluation of the photometric stability for the OST transit spectrograph are as follows:

1. Incident flux including transit signal, f, is decomposed into average and variation terms: $f(t) = \langle f \rangle_t + \delta f(t)$. The variation term does not include the surface brightness fluctuation due to stellar activity.
2. Bias voltage is common to all pixels.
3. Three offset voltages, $V_{cv,i}$, $V_{mux,j}$, and $V_{read,j}$, do not change over time.
4. The conversion factor from electric charge to voltage, g_i, depends on capacitance of condenser and bias voltage. While the capacitance does not change, the bias voltage is changed over time. As a result, the fluctuation of conversion factor is determined by the bias voltage, which is common to all the detector pixels.
5. Individual amplitude gains occurred in the detector, multiplexer, and readout electronics, $g_{det,i}$, $g_{mux,j}$, and $g_{read,j}$, are statistically independent.
6. Digitalization noise occurred by analog to digital conversion, σ_{AD}, is included in readout noise.

E2. Parameters

Parameters used for formulation of the science pixel and reference pixel (shielded from any thermal source) are compiled in Table E1. Through this document, fluctuation of parameter *A* and average of parameter *A* over parameter *B* are represented by δA and $\langle A \rangle_B$, respectively. σ_A is the standard deviation of parameter *A*. $\tilde{A}$ represents normalized parameter *A*.

Table E1. Definition of parameters

Symbol	Unit	Meaning
a	[radian]	field stop radius
D	[cm]	telescope diameter
$D_{onref,i,j}$	[V]	value of the *i*-th onboard reference pixel with the *j*-th multiplexer and readout electronics. $D'_{onref,i,j}$ is its pixel value without the *i*-th offset voltage.

$D_{outref,i,j}$	[V]	value of the *i*-th outboard reference pixel with the *j*-th multiplexer and readout electronics.
$D_{signal,i,j}$	[V]	value of transit signal on the *i*-th science pixel with the *j*-th multiplexer and readout electronics
$D_{sub,bin}$	[V]	binning data of $D_{sub,i,j}$ (sum of the n_{sci} science pixel values).
$D_{sub,i,j}$	[V]	value of subtraction of $D'_{onref,i,j}$ from $D'_{sci,i,j}$.
$D_{sci,i,j}$	[V]	value of the *i*-th science pixel with the *j*-th multiplexer and readout electronics. $D'_{sci,i,j}$ is its subtracted value from the *i*-th offset voltage
$D_{sci0,i,j}$	[V]	ideal value of the *i*-th science pixel with the *j*-th multiplexer and readout electronics.
f	[/pixel/sec]	number of the incident photons into a sub-region of the primary mirror corresponding to one detector pixel
g_{com}		fluctuation of detector gain common to all pixels
$g_{cv,i}$		conversion factor from electric charge to voltage attached to the *i*-th pixel
$g_{mux,j}$		amplitude gain of the *j*-th multiplexer
$g_{read,j}$		amplitude gain of the *j*-th readout electronics
k	[cycle/pupil]	absolute value of wave number of phase fluctuation
L		photometric value (δL is photometric variance)
N_{motion}		number of pixels newly irradiated or not newly irradiated by image motion
n_{ref}		number of reference pixels
n_{sci}		number of science pixels irradiated by a same spectral component
O_i		optical transmissivity including quantum efficiency attached to the *i*-th pixel
PSD	[radian^2/(cycle/pupil)^2]	power spectral density of high order aberration
PSF_0		ideal PSF intensity distribution without optical phase aberration
PSF_ψ		PSF intensity distribution with optical phase aberration
Q_{com}	[e-]	fluctuation of dark current common to all pixels
Q_i	[e-]	electrical charge of the *i*-th pixel when no light enters its pixel (corresponding to dark current)
r		radial direction on focal plane
S		Strehl ratio
t	second	time
T_{det}	[K]	temperature of detector
T_{warm}	[K]	temperature of warm electronics

V_b	[V]	bias voltage common to all the pixels
$V_{cv,i}$	[V]	offset voltage of the *i*-th pixel generated in conversion process from current to voltage
$V_{i,j}$	[V]	total amount of offset voltage generated in the *i*-th pixel with the *j*-th multiplexer and readout electronics
$V_{mux,j}$	[V]	offset voltage generated in the *j*-th multiplexer
$V_{read,j}$	[V]	offset voltage generated in the *j*-th readout electronics
(x, y)		Cartesian coordinates of a focal plane
$\Delta\theta$		telescope pointing jitter
λ	[cm]	wavelength
σ_{AD}	[V]	quantization noise
σ_{dark}	[V]	shot noise of dark current attached to the *i*-th pixel
σ_{inter}		standard deviation of inter-pixel sensitivity variation
$\sigma_{onref,i,j}$	[V]	random noise of the *i*-th onboard reference pixel with the *j*-th multiplexer and readout electronics
$\sigma_{outref,i,j}$	[V]	random noise of the *i*-th outboard reference pixel with the *j*-th multiplexer and readout electronics
$\sigma_{photon,i}$	[V]	shot noise of incident photon attached to the *i*-th pixel
$\sigma_{sci,i,j}$	[V]	total amount of noise for the *i*-th science pixel with the *j*-th multiplexer and readout electronics
$\sigma_{read,j}$	[V]	readout noise for the *j*-th readout electronics
τ		optical transmittance of mask